1 **Delayed Stormflow Generation in a Semi-humid Forested Watershed**

2 **Controlled by Soil Water Storage and Groundwater**

3 Zhen Cui, Fuqiang Tian[*]

4 Department of Hydraulic Engineering, State Key Laboratory of Hydroscience and Engineering,

5 Tsinghua University, Beijing 100084, China.

6

7

8 Corresponding author: Fuqiang Tian (tianfq@tsinghua.edu.cn)

9 **Key Points:**

10 • Delayed stormflow is initiated when soil water content reaches field capacity.

11 • Groundwater levels dictate the timing and magnitude of delayed stormflow.

12 • Rising groundwater levels enhance hydraulic conductivity and hydrologic connectivity,

13 driving delayed stormflow.

14

15   **Abstract**

16   An analysis by Cui et al. (2024) of stormflow responses to rainfall in a mountainous forested

17   watershed in the semi-humid regions of North China identified a distinct threshold for bimodal

18   rainfall-runoff events, where delayed stormflow appeared to be influenced by shallow groundwater.

19   This study further investigates the processes driving these bimodal events, focusing on the dynamics

20   of soil water content (SWC) and groundwater level (GWL) during storm events. The results show

21   that delayed stormflow is governed by the interplay between SWC and GWL. Delayed stormflow is

22   initiated when SWC exceeds the soil's water storage capacity, while its timing and volume are

23   determined by GWL fluctuations. During rainfall, SWC increases rapidly; if it does not reach the

24   soil's water-holding capacity, it stabilizes after the rainfall ends. Conversely, if SWC surpasses the

25   soil's storage capacity, it decreases rapidly post-rainfall, with the excess rainwater infiltrating deeper

26   to recharge groundwater, leading to a gradual rise in GWL. As GWL rises, increased hydraulic

27   conductivity facilitates the movement of shallow groundwater into the stream channel, resulting in

28   delayed stormflow. Simultaneously, the effective connection area between the stream channel and

29   adjacent hillslopes expands vertically. At specific high GWL thresholds, GWL responses across the

30   watershed converge, significantly increasing groundwater discharge and reducing lag times, often

31   causing the delayed stormflow peak to merge with the direct stormflow peak. These findings enhance

32   our understanding of delayed stormflow generation in similar regions and contribute to refining runoff

33   generation theories.

34   **Keywords:** Delayed stormflow; Soil water storage; Groundwater outflow; Stormflow generation

35   mechanism; Hydraulic conductivity

36   **1. Introduction**

37   Previous research on stormflow processes in the Xitaizi Experimental Watershed (XEW) in

38   North China identified a frequent occurrence of bimodal stormflow hydrographs, which often result

39   in significant stormflow and associated flooding. Our findings highlighted that the onset of these

40 bimodal hydrographs is governed by threshold behavior, with delayed streamflow peaks emerging

41 when the combined total of event rainfall and antecedent soil moisture index exceeds 200 mm.

42 Additionally, we determined that delayed stormflow is primarily driven by contributions from shallow

43 groundwater. However, the mechanisms underlying the development of these bimodal hydrographs,

44 which represent complex emergent hydrological behaviors, remain poorly understood. Gaining

45 insight into the formation of delayed stormflow is crucial for advancing our understanding of

46 catchment runoff generation processes and improving flood forecasting capabilities.

47   Bimodal streamflow responses typically occur during the wetting-up phases of catchments.

48 Extensive research has examined the factors influencing dual streamflow peaks, revealing that

49 bimodal hydrographs are associated with threshold behavior linked to antecedent soil moisture,

50 antecedent precipitation, groundwater levels, soil water storage, and rainfall amount (Haga et al.,

51 2005; Graeff et al., 2009; Anderson and Burt, 1978; Padilla et al., 2015; Martínez-Carreras et al.,

52 2016). Despite these findings, the specific reasons for such threshold behavior—and how it leads to

53 the diverse shapes of stormflow hydrographs—remain inadequately explained. For instance,

54 Martínez-Carreras et al. (2016) documented a delayed peak only when watershed storage reached a

55 critical threshold of 113 mm. However, the precise reasons for this threshold and the processes that

56 follow are not fully understood.

57   The bimodal hydrograph is a significant manifestation of the nonlinear runoff response,

58 reflecting the complex interactions between runoff and rainfall. This nonlinear pattern provides

59 valuable insights into stormflow processes, including both the timing and magnitude of the response.

60 Recent decades have seen an increase in research on nonlinear and threshold changes in rainfall-

61 runoff responses, contributing to a deeper understanding of stormflow generation mechanisms.

62 Nonlinear shifts in stormflow, often characterized by rapid responses that can lead to flooding, have

63 been extensively documented (Detty and McGuire, 2010; Farrick and Branfireun, 2014; Graham et

64 al., 2010; Tromp-van Meerveld and McDonnell, 2006a; Penna et al., 2011; Scaife et al., 2020).

65 However, much of the existing literature lacks detailed exploration of the intricate mechanisms that

66 govern these shifts and the subsequent post-threshold runoff processes, leaving a gap in our

67   understanding of these complex hydrological dynamics across diverse catchments.

68   Bimodal runoff processes exemplify a typical nonlinear response of runoff, offering an intuitive

69   and effective way to simplify the description of complex hydrologic systems. Despite this, many

70   studies fail to distinguish between unimodal and bimodal streamflow responses, limiting our

71   understanding of these phenomena. Therefore, an in-depth investigation into the mechanisms driving

72   these responses is essential. Such research would enable the grouping of similar hydrologic responses

73   and facilitate comparisons of stormflow generation processes across different watersheds (Graham

74   and McDonnell, 2010; Tromp-van Meerveld and McDonnell, 2006a, b).

75   Observing substantial stormflow events in semi-humid regions is challenging due to the

76   relatively arid climate and lower runoff coefficients. Over the past decade, our analysis of 15 bimodal

77   stormflow events has provided valuable data and insights, contributing to the advancement of runoff

78   generation studies in similar regions. This study focuses on the dynamics of SWC and GWL to

79   investigate the processes underlying delayed stormflow patterns. The primary objectives are: (1) to

80   analyze the dynamics of SWC and GWL during storm events, (2) to elucidate the intrinsic

81   mechanisms driving the threshold behavior in bimodal hydrograph processes, and (3) to reveal the

82   generation mechanisms of delayed stormflow within the Xitaizi Experimental Watershed.

83   ## 2. Materials and methods

84   ### 2.1 Study site

85   The study was conducted in the Xitaizi Experimental Watershed (XEW), a small catchment in

86   North China, located approximately 70 km northeast of Beijing at coordinates 40°32′N and 116°37′E

87   (Fig. 1). XEW covers an area of 4.22 km², with elevations ranging from 676 to 1201 m above sea

88   level. The watershed is characterized by a monsoon-influenced semi-humid climate, with an average

89   annual precipitation of 625 mm, 80% of which occurs from June to September. The mean annual

90   temperature is 11.5°C, and the average relative humidity is 59.1%.
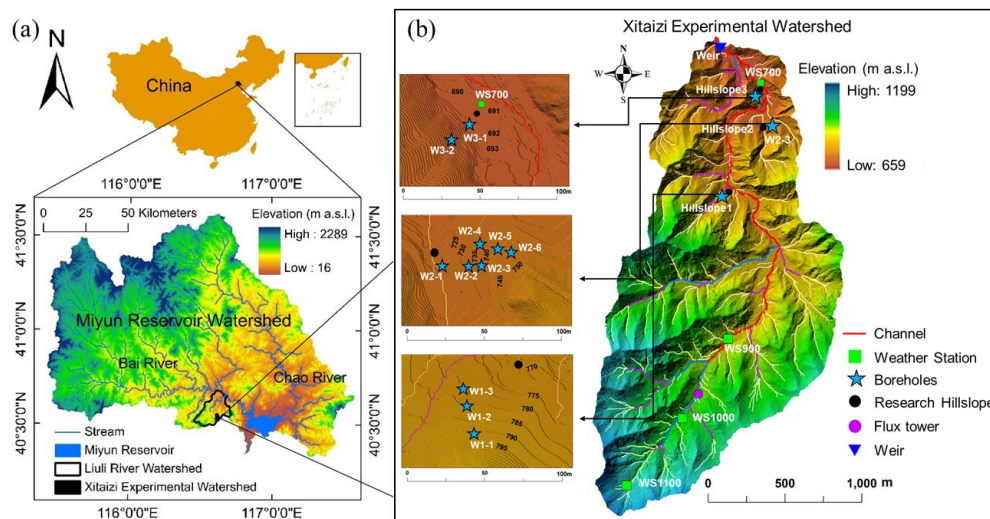
Figure 1. Location of Xitaizi Experimental Watershed (XEW), and the detailed distributed monitoring stations and instruments, including four weather stations, an outlet weir, eleven groundwater boreholes and five soil water profiles.

The geology of XEW is dominated by firmly compacted, deeply weathered granite, accounting for approximately 80% of the catchment area. The remaining bedrock consists of gneiss and dolomite. The watershed's soil types, primarily brown earth and cinnamon soil, extend to a depth of 1.5 meters with a saturated hydraulic conductivity ranging from 19.5 to 175.3 mm/h, averaging 45 mm/h. The catchment is heavily forested, with 98% coverage, comprising 54.2% broad-leaved, 2.3% coniferous, and 10.5% mixed forests. Shrubs cover the remaining 33% of the land.

2.2 Meteorological and hydrological measurements

Meteorological data were collected from 2013 to 2023 using four GRWS100 automatic weather stations, strategically distributed along an elevation gradient within XEW (Fig. 1). Air temperature and relative humidity were monitored using HC2S3-L probes, equipped with radiation shields, while photosynthetically active radiation was measured with LI-190R quantum sensors. Rainfall was recorded at 10-minute intervals using six tipping-bucket rain gauges located in open areas near the weather stations, with data averaged for analysis.

108   Streamflow was measured at the catchment outlet using a Parshall flume, with water levels

109   recorded every 5 minutes by a HOBO capacitance water level logger from 2014 onwards. The

110   recorded data were averaged to hourly intervals for analysis. Due to environmental challenges, some

111   data were lost, including stormflow data from July 19 to August 16, 2016, and streamflow data from

112   2018 to 2019, resulting in the exclusion of certain events from the analysis.

2.3 Soil Water Content Observation

114   Volumetric soil water content (SWC) was monitored using CS616 time-domain reflectometry

115   (TDR) probes at eight locations within the watershed. Data were recorded at 10-minute intervals,

116   with five sensors installed on Hillslope 1 and three near WS900 at 80 cm depth intervals. For this

117   study, the measurements were aggregated to hourly time steps, and the arithmetic mean SWC across

118   the profiles was used for analysis.

2.4 Groundwater Level Observation

120   Groundwater levels (below the ground surface, hereinafter referred to as bgs) were observed in

121   eleven 80 mm diameter boreholes distributed across three hillslopes within XEW (Fig. 1). Borehole

122   depths ranged from 5 to 26 m, penetrating weathered and fractured granite with varying degrees of

123   soil mantling. HOBO capacitance water level loggers recorded hourly groundwater levels. Boreholes

124   W1-1, W1-2, W2-4, W2-5, and W2-6 frequently registered no water levels, potentially due to

125   insufficient drilling depth. The saturated hydraulic conductivity of the weathered and fractured granite

126   was estimated to range from 5.2×10^{-3} m/day to 1.16 m/day based on slug tests.

127   Groundwater levels were normalized using an index (I_G) calculated for each borehole following

128   the approach by Detty and McGuire (2010). The arithmetic mean of IG across all boreholes was used

129   to represent the overall groundwater level in the watershed.

2.5 Separation of Rainfall-Runoff Events

131   Rainfall events were identified using an intensity-based automatic algorithm described by Tian

132   et al. (2012). This algorithm defines event start and end times based on a threshold rainfall intensity

133   of >0.1 mm/h, with a minimum separation of six hours between events. Only events with cumulative

134   rainfall exceeding 5 mm were included in the analysis, resulting in the identification of 95 distinct

135   rainfall events from 2014 to 2023.

136   Storm runoff events were defined by a rapid streamflow increase and peak following rainfall.

137   Streamflow hydrographs were separated into baseflow and stormflow components using the HYSEP

138   program (Sloto & Crouse, 1996), with manual verification and adjustment based on straight-line

139   separation principles.

2.3 Rainfall-runoff event analysis

141   The analysis focused on understanding the conditions under which subsurface flow connects to

142   or disconnects from the stream. The dynamics among streamflow, SWC, and GWLs were examined

143   to reveal connectivity patterns, providing insights into the underlying processes. This simultaneous

144   observation of soil water, groundwater, and streamflow is defined as the soil water-groundwater–

145   stream response relationship.

146   Rainfall-runoff events, defined as those with total rainfall exceeding 5 mm and a corresponding

147   peak in streamflow, were analyzed. The peak rainfall intensity (R_p) was determined based on the

148   maximum 1-hour rainfall intensity, with the time of occurrence recorded as TP_p. As illustrated in Fig.

149   2, the initial streamflow (Q_0) was defined as the streamflow just before it began to rise, and TQ_p was

150   the time when the maximum streamflow (Q_p) occurred. TRs and TR_e represent the start and end times

151   of rainfall, respectively. The analysis of SWC and GWL dynamics followed a similar approach to

152   streamflow, replacing Q_0 and TQ_p with SWC_0 (I_{G0}) and TS_0 (TI_{G0}), and SWC_p (I_{Gp}) and TS_p (TI_{Gp}),

153   respectively. This study analyzed 95 distinct rainfall-runoff events to better understand the

154   interactions between soil water, groundwater, and streamflow in response to rainfall.
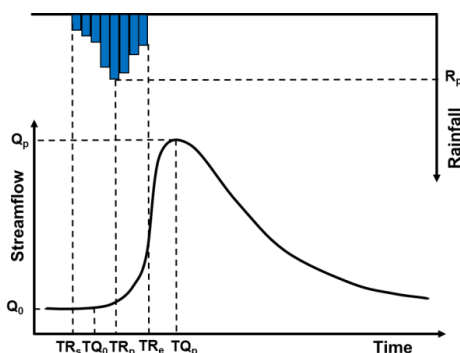
Figure 2. Definition sketch for analysis of rainfall event.

3. Results

3.1. Relationship between SWC and GWL variability at the hillslope scale

We conducted a detailed analysis of the temporal evolution of SWC and GWL at the hillslope scale, focusing on their interactions across 95 rainfall-runoff events. Our analysis revealed a strong correlation between increases in GWL and elevated SWC values. During the early stages of these events, rainfall prompted a rapid rise in SWC, while GWL remained relatively stable. Once SWC reached a certain threshold, it either plateaued or gradually declined, coinciding with a marked increase in GWL. Subsequently, both SWC and GWL exhibited a nearly synchronous decline as GWL reached specific levels, manifesting in three distinct patterns of variation.

Figure 3 illustrates the response characteristics of SWC and GWL during three representative events. Red circles indicate periods of rainfall, while black circles represent post-rainfall periods. In a typical light rainfall event, as shown in Fig. 3a, the soil remained relatively dry with SWC values mostly below 0.20. During rainfall, SWC increased steadily until the rainfall ceased, after which it stabilized, while GWL showed minimal change.

8
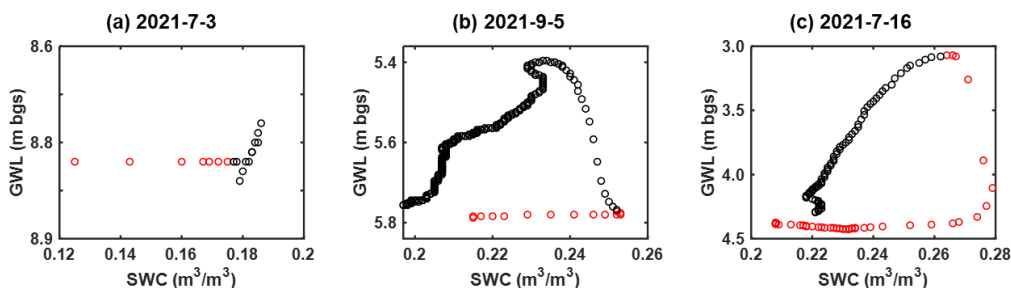
Figure 3. Three typical SWC-GWL dynamics patterns during rainfall-runoff events.

Figures 3b and 3c depict the dynamics of SWC and GWL during storm events, where a pronounced counterclockwise hysteretic relationship was observed. Both SWC and GWL exhibited significant increases, with SWC surpassing 0.20. The primary distinction between these patterns lies in the timing of the GWL rise: in Fig. 3b, GWL began to rise after the rainfall ended, whereas in Fig.3c, GWL started to rise noticeably before the end of the rainfall.

In the scenario represented by Fig. 3b, SWC continued to rise during rainfall while GWL remained largely unchanged. After the rainfall ceased, SWC began to decline, and GWL subsequently rose before eventually falling. Fig. 3c, which typically represents extreme storm events, shows that when SWC exceeded 0.25, GWL rose sharply as SWC continued to increase until it reached 0.28. Despite ongoing rainfall, SWC then decreased, and GWL experienced a significant surge, continuing until the rainfall stopped, after which both variables began to decline. This pattern underscores the complex dynamics of SWC and GWL during storm events, highlighting the nuanced responses of these hydrological parameters.

We further quantified the frequency of SWC and GWL increases or decreases across the 95 rainfall-runoff events. As depicted in Fig. 4, there were 49 events where SWC increased and 43 events where GWL increased. Among these, 26 events saw a decline in SWC, and 15 experienced a decline in GWL, with only 15 events showing a decrease in both variables. These 15 events were associated with delayed stormflow and generated larger stormflow volumes. Notably, the rainfall-runoff event on August 15, 2021, featured a more dispersed rainfall distribution, with multiple fluctuations in SWC and GWL throughout the event. Consequently, our subsequent analysis primarily focused on the

193   remaining 14 events.
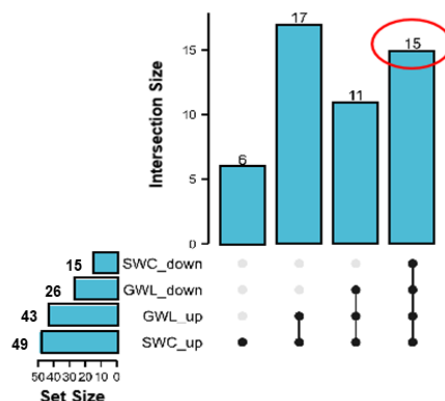
194

195   **Figure 4**. Upset plot of soil water content and groundwater level response characteristics.

196   **3.2 Soil water content dynamics during storm events**

197   Figure 5 presents the SWC dynamics observed during 14 distinct rainfall-runoff events, each

198   characterized by minimal or no intermittent rainfall during the recession period. To facilitate a clear

199   comparison of SWC changes across different events, the peaks of all events were aligned to the

200   position corresponding to a horizontal axis value of 0.

201   During the initial phases of these events, rainfall triggered a rapid increase in SWC, which

202   quickly reached its peak. In the recession phase, the rate of SWC decline slowed as SWC decreased,

203   eventually stabilizing around 0.20. This pattern of SWC variation is schematically represented in Fig.

204   6.

205
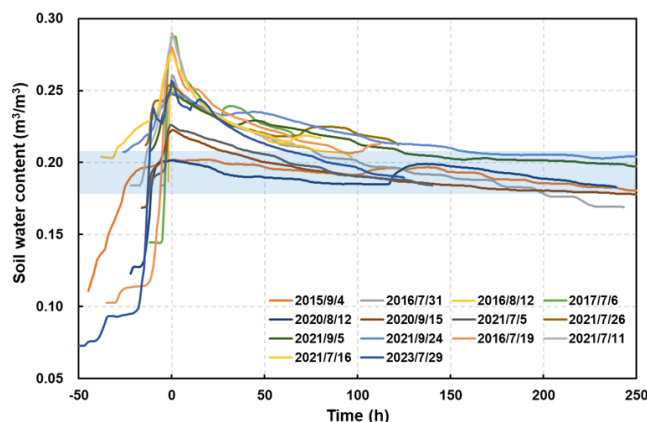
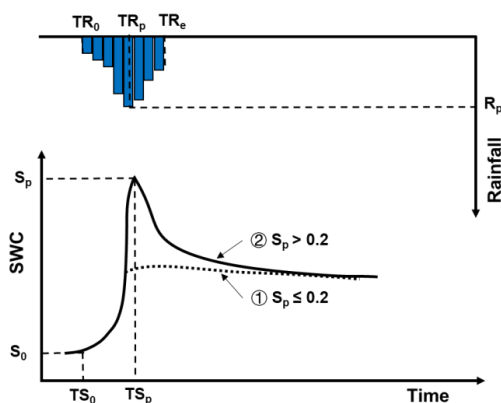**Figure 5.** Soil water content dynamics during various storm events.

The SWC response to rainfall was found to be extremely rapid. Upon the onset of rainfall, SWC quickly increased. Once the rainfall ceased, the subsequent behavior of SWC was dependent on its peak value. If SWC was less than or equal to 0.20, it either stabilized for a period or decreased very slowly. However, if SWC exceeded 0.20, it decreased rapidly, eventually stabilizing around 0.20. The presence of a peak in SWC was determined by whether it surpassed the 0.20 threshold; the greater the excess above 0.20, the more rapid the subsequent decline.


213

Figure 6. Schematic diagram of soil water content response process during storm events. S_p is the maximum value of soil water content.

3.3 GWL dynamics during storm events

During storm events, we identified two distinct types of GWL responses: quick and slow. These response types are conceptually illustrated in Fig. 7. The GWL with a quick response typically exhibits a distinct process curve compared to the slower response. The quick GWL response is closely aligned with a swift increase in soil water content (SWC), lagging the SWC peak by just 0 to 6 h (Fig. 7a). In scenarios where SWC exceeds 0.20, particularly beyond 0.24, the GWL often shows a secondary increase following its initial peak, marked by the dotted line in Fig. 7a. Conversely, a slower GWL response, depicted in Fig. 7b, occurs when SWC declines sharply after peaking.

Analysis of GWL variations across hillslope positions revealed that GWL in HS2 (W21-23) exhibits the rapid response type (Fig. 7a), while GWL in HS1 (W13) and HS3 (W31 and W32) demonstrates the slower response type (Fig. 7b). These response patterns suggest that the GWL dynamics are not only influenced by SWC but are also dependent on the specific hillslope's geological structure.
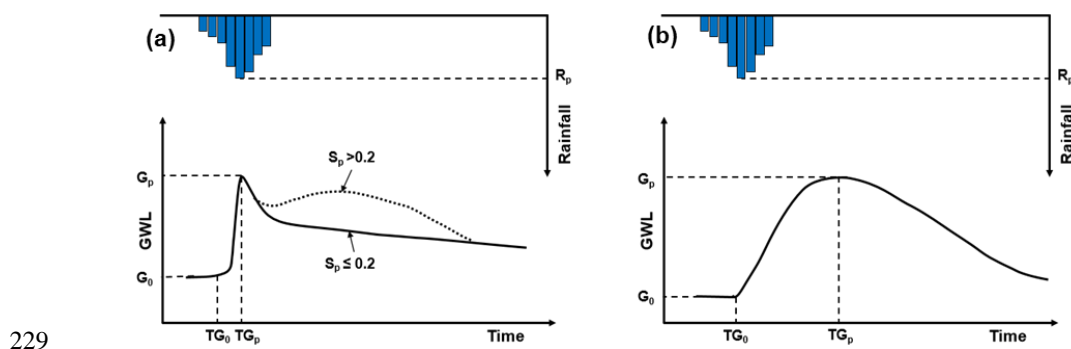
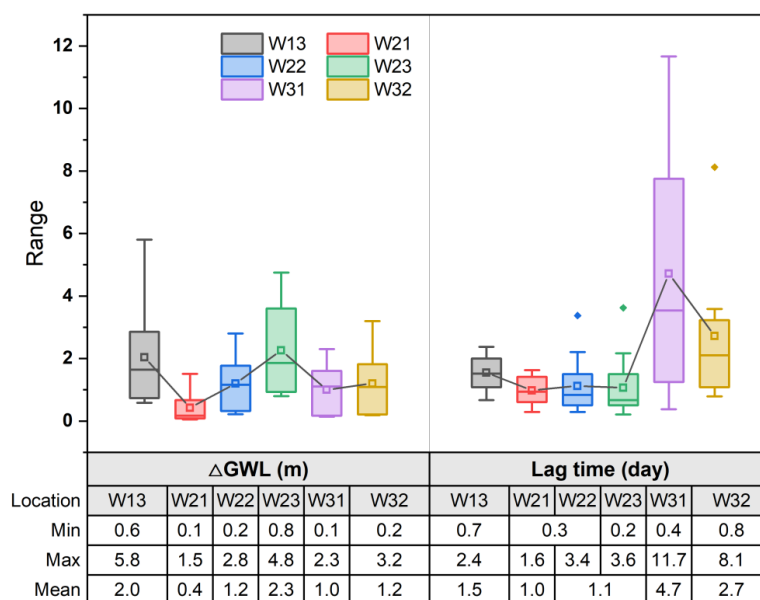**Figure 7.** Schematic diagram of groundwater level response during storm events. G_0 and G_p are the initial and maximum values of groundwater level respectively. S_p is the maximum value of soil water content.

Further examination of GWL responses at various locations is presented in Fig. 8, which details the magnitude of GWL increases and the lag times relative to rainfall onset for each event. Despite

12

235 variability in GWL across observation wells, with the exception of W21 and W31 (which are located

236 at the foot of the hillslope and exhibit smaller GWL changes), the differences in GWL increments at

237 other wells are relatively minor, with mean increases ranging from 1 to 2 meters. On the same

238 hillslope, GWL increments generally increase progressively from the foot to the top (e.g., W21, W22,

239 and W23 on HS2, and W31 and W32 on HS3).

Location	ΔGWL (m)						Lag time (day)					
	W13	W21	W22	W23	W31	W32	W13	W21	W22	W23	W31	W32
Min	0.6	0.1	0.2	0.8	0.1	0.2	0.7	0.3		0.2	0.4	0.8
Max	5.8	1.5	2.8	4.8	2.3	3.2	2.4	1.6	3.4	3.6	11.7	8.1
Mean	2.0	0.4	1.2	2.3	1.0	1.2	1.5	1.0		1.1	4.7	2.7

240

241 **Figure 8.** Groundwater level increments (ΔGWL) and lag time of peak water level relative to
242 rainfall onset across locations.

243   However, lag times for reaching maximum GWL exhibit greater variation across locations. For

244 instance, at HS3, the delay for maximum GWL in W31 ranged from 0.4 to 11.7 days, and in W32

245 from 0.8 to 8.1 days, both of which are longer than the lag times observed at HS1 (0.7 to 2.4 days)

246 and HS2 (0.2 to 3.6 days). There is no clear correlation between the lag time of maximum GWL and

247 its distance from the hillslope foot within the same hillslope. These discrepancies in lag times between

248 different hillslopes may be attributed to spatial variations in geological conditions, as suggested by

249 Kosugi et al. (2011) and Padilla et al. (2015).

13

3.4 Characterization of GWL response on different hillslopes

Figure 8 reveals that while the magnitude of GWL increments across various locations remains relatively consistent, the lag time for GWL to reach its maximum value exhibits substantial variation. To further investigate these dynamics, we analyzed the relationship between GWL increments and SWC across 14 storm events. In Fig. 9, the length of the orange bar represents the GWL increment during the phase when SWC increased to its peak, while the green bar indicates the GWL increment during the phase when SWC decreased from its peak until GWL reached its maximum. The black and red dotted lines mark the initial SWC and the SWC at the onset of GWL rise, respectively. Locations without bars in Fig. 9b, e, and f indicate missing data.

The analysis shows that a significant increase in SWC from its initial value following rainfall is indicative of a delayed GWL response. Specifically, the larger the difference between the SWC at the onset of GWL rise (SWC_G) and the initial SWC (SWC_0), the later the GWL rise begins. Conversely, if SWC_G and SWC_0 are closely aligned, the GWL begins to rise almost simultaneously with the increase in SWC.

For example, at HS1 (W13), GWL began to rise only after SWC exceeded 0.20, and the majority of the GWL increase occurred during the SWC decline phase. This suggests that the GWL response on HS1 is influenced by soil wetness, indicating a potential threshold effect of SWC on GWL dynamics. On HS2 (including W21-23), the GWL response was more immediate, with increases closely following SWC rises. Here, the SWC at the onset of GWL rise varied widely, ranging from 0.13 to 0.26, and was generally close to the initial SWC, suggesting that GWL increases at these locations are less dependent on SWC thresholds. HS3 exhibited both quick and slow GWL responses. The initial response occurred soon after the SWC increase but at a slow rate that persisted over an extended period. The majority of the GWL increment at HS3 occurred during the SWC decline phase after its peak.
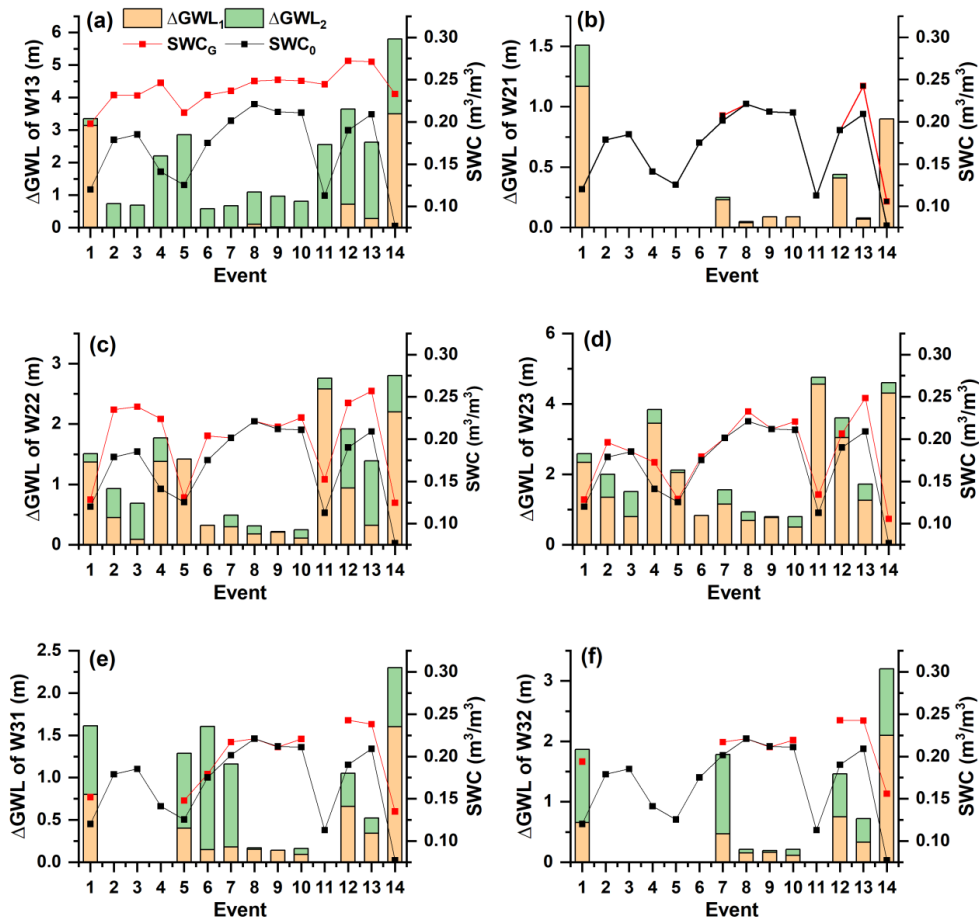
Figure 9. Groundwater level increments (ΔGWL) across various locations during 14 storm events, along with initial soil water content (SWC_0) and corresponding soil water content at groundwater level initiation (SWC_G).

These findings indicate that the emergence of quick and slow GWL response types is strongly linked to SWC dynamics. In quick response types, GWL growth primarily occurs during the SWC increase phase, resulting in a steep response curve. In slow response types, GWL growth predominantly occurs during the SWC decline phase after the peak, leading to an arch-shaped response curve. This distinction underscores the critical role of SWC dynamics in governing the timing and magnitude of GWL responses across different hillslopes.

3.5 Inter-hillslope dynamics in GWL response

284

285   To explore the differences in GWL response times across hillslopes, particularly the delayed

286   occurrence of maximum GWL on HS3 compared to HS1 and HS2, we quantified the lag times of

287   GWL responses on HS1 (t_{S1}), HS2 (t_{S2}), and HS3 (t_{S3}) relative to the onset of rainfall. We then

288   calculated the elapsed time differences between t_{S1} and t_{S3}, as well as between t_{S2} and t_{S3} ($\Delta t = t_S - t_{S3}$)

289   and analyzed their correlation with peak I_G, as shown in Fig. 10. Negative Δt values indicate that the

290   GWL peaks on HS1 and HS2 occurred earlier than on HS3.

291   A significant negative linear relationship was observed between Δt and peak I_G, described by the

292   equation $I_G = -0.0015 \times \Delta t + 0.27$ ($R^2 = 0.78$, $p < 0.001$). As GWL increased , eventually approaching

293   zero when peak I_G exceeded 0.30, with only minor fluctuations, particularly during extreme storm

294   events. Notably, although Fig. 10 labels the vertical axis as I_G to represent watershed GWL status, a

295   similar pattern emerges when replacing c with GWL at any specific location, though the GWL

296   thresholds vary across different sites.

297
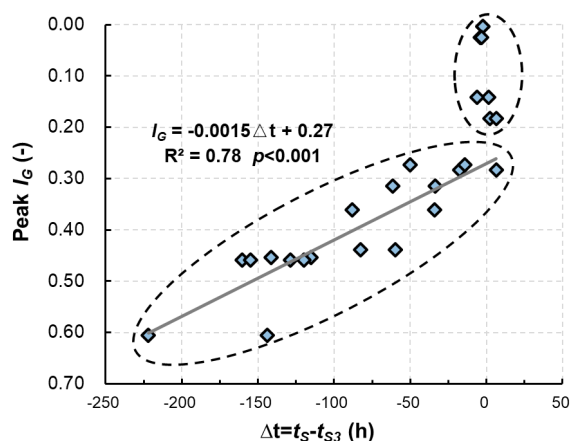
Figure 10. Correlation between peak I_G and the elapsed times from t_{S1}, t_{S2} to t_{S3} ($\Delta t = t_S - t_{S3}$). t_{S1}, t_{S2}

299   and t_{S3} are the lag time of peak groundwater levels on HS1, HS2 and HS3, respectively.

300   These results suggest that as GWL increases, the GWL response across different hillslopes tends

301   to synchronize. This synchronization may be attributed to the enhanced hydraulic conductivity as

302   GWL rises, as noted by Padilla et al. (2015), who reported that shorter lag times in bedrock

303   groundwater are associated with high-transmissivity conduits. When a critical GWL threshold is

304   reached, the water transport capacity increases substantially, leading to nearly simultaneous responses

305   across hillslopes. This finding is consistent with Scaife et al. (2020), who observed increased

306   hydrological connectivity between hillslopes and the stream channel during such conditions.

307   In summary, these results indicate that as GWL rises, not only does groundwater recharge more

308   rapidly from infiltrating rainfall, but it also reaches the stream channel more quickly through more

309   transmissive layers, which can be explained by the transmissivity feedback mechanism (Kendall et

310   al., 1999; Bishop et al., 2011).

4. Discussion

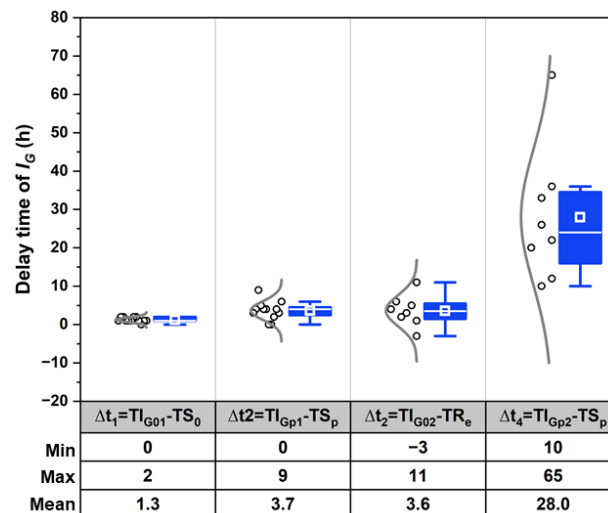### 4.1 Characterization of groundwater response at the watershed scale

313   The groundwater level (GWL) response to storm events exhibited spatial variability across the

314   watershed. I_G, which represents the average normalized GWL across different locations, provides a

315   comprehensive view of the watershed's GWL dynamics. Our analysis of I_G revealed that, compared

316   to individual well GWL changes, I_G often exhibits two distinct peaks during storm events. Specifically,

317   among the 14 events analyzed, 9 events showed two I_G peaks, which coincided with the occurrence

318   of two streamflow peaks. In contrast, only wells W13 and W23 exhibited dual GWL peaks: W13

319   displayed two peaks during one event, while W23 exhibited two peaks in five events, with the

320   remaining wells showing only a single peak (see Table 1).

321   **Table 1.** Statistical results of response characterization of streamflow, I_G and groundwater levels.

			HS1		HS2		HS3	
	Streamflow	I_G	W13	W21	W22	W23	W31	W32
Total number of events	14	14	14	8	14	14	9	9
Number of events with two peaks	9	9	1	0	0	5	0	0

Figure 11 illustrates the timing of I_G peaks relative to the soil water content (SWC) response. The first I_G peak occurred rapidly following rainfall, initiating 0-2 h after the SWC began to rise and peaking 0-9 h later (average 3.7 h) after the SWC reached its maximum. The second I_G peak typically occurred post-rainfall, lagging behind the SWC peak by 10-65 h (average 28 h). These response patterns are consistent with the quick and slow GWL response types identified in section 3.2. The occurrence of two I_G peaks is primarily attributed to the superimposition of groundwater contributions from different hillslopes, each with distinct response rates. The fast GWL response is closely linked to immediate rainfall and rising SWC, whereas the slow GWL response occurs over a broader timescale, emphasizing the need for further attention to the latter in hydrological studies.


	$\Delta t_1 = TI_{G01} - TS_0$	$\Delta t2 = TI_{Gp1} - TS_p$	$\Delta t_2 = TI_{G02} - TR_e$	$\Delta t_4 = TI_{Gp2} - TS_p$
Min	0	0	−3	10
Max	2	9	11	65
Mean	1.3	3.7	3.6	28.0

Figure 11. Delay time of I_G peaks relative to peak soil water content. TI_{G01} and TI_{G02} are the onset times of the first and second peaks of I_G, respectively. TS_0 and TS_p are the time when soil water content started to increase and peaked, respectively. TI_{Gp1} and TI_{Gp2} are the time when I_G started to increase and peaked, respectively. TR_e is when the rainfall ends.

The growth rates of I_G towards the two peaks in various events were quantified (Fig. 12). A notable disparity was observed between the growth rates of the two peaks, with the first peak (r_1) displaying a significantly higher rate than the second peak (r_2). Specifically, r_1 ranged from 0.03 to

339   0.98 per day (average 0.38/day), while r_2 ranged from 0.01 to 0.31 per day (average 0.07/day). These

340   two peaks correspond to the quick and slow GWL responses across different hillslopes. In events

341   featuring two I_G peaks, the maximum I_G typically occurred at the second peak. Additionally, in events

342   characterized by higher GWLs (lower I_G), the difference between the growth rates of the two I_G peaks

343   diminished, making them more difficult to distinguish, as observed in events 9 and 10. In events 11-

344   14, which had much higher GWLs, only a single peak was observed in the I_G process. This outcome

345   aligns with the findings presented in Fig. 10, indicating that higher GWLs lead to a more synchronized

346   GWL response across the watershed.
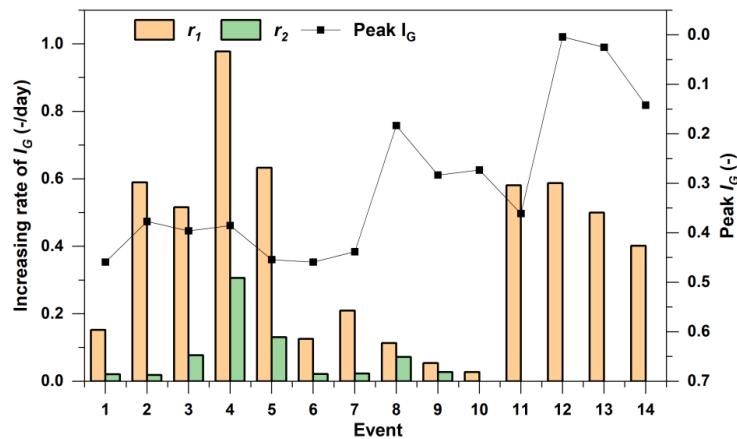
Figure 12. Growth rates of I_G and its maximum value across various events. r_1 and r_2 denote the rates of ascent during the periods when I_G reaches its first and second peaks, respectively.

350   The first I_G peak, which occurred rapidly during rainfall and was closely associated with rising

351   SWC, contrasts with the second I_G peak, which appeared post-rainfall when the soil layer began

352   draining. The formation processes and underlying mechanisms of these two I_G peaks are distinct. As

353   Dang et al. (2023) noted, rainfall generates pressure waves that rapidly expel soil water from the

354   column's bottom, while infiltrated rainwater migrates slowly downward. This change in head within

355   the surface soil layer can induce an immediate GWL response. We hypothesize that the fast I_G peak

356   may result from increased SWC inducing a kinematic wave, which displaces "old" soil water and

357   groundwater ahead, leading to a near-synchronous GWL rise (e.g., Anderson and Burt, 1978).

358   Although water flow through soil and bedrock is slow, the theoretical celerity of this response is

359   instantaneous, hence the rapid GWL rise. Furthermore, early drilling data revealed the presence of

360   faults in the rock structure of HS2, which may contribute to the faster GWL response on this hillslope

361   compared to others. The slow I_G peak likely forms as rainwater gradually infiltrates through the soil

362   and bedrock layers, eventually recharging the groundwater. Crucially, there exists a threshold for the

363   soil layer's water storage capacity: before SWC reaches this threshold, all rainfall is retained within

364   the soil layer. Once this critical threshold is surpassed, the soil layer cannot retain additional water

365   for extended periods and swiftly releases excess water to deeper layers, leading to a subsequent

366   reduction in SWC while the GWL rises due to effective groundwater replenishment from infiltrated

367   rainwater.

368   **4.2 Delayed stormflow processes dynamically aligned with GWL dynamics**

369   Previous studies (Cui et al., 2024) indicated that during heavy rainfall, the streamflow in the

370   XEW exhibits a bimodal hydrograph, with delayed stormflow likely formed by shallow groundwater

371   outflow. Assessing the relative timing and lags between groundwater and streamflow responses is

372   crucial for understanding dominant runoff generation processes (Beiter et al., 2020). Inconsistencies

373   in response times may indicate the contribution of alternative water sources to the stream channel.

374   Fig. 13 illustrates the timing of maximum I_G ($I_{G\text{p}}$) and maximum SWC (SWC_p) responses for eight

375   storm events, as well as the rainfall duration. Each horizontal bar represents the onset of rain on the

376   left end and the lag time for the maximum value on the right end of the corresponding variable, except

377   that the bar length for t_Rain indicates the duration of the rainfall.
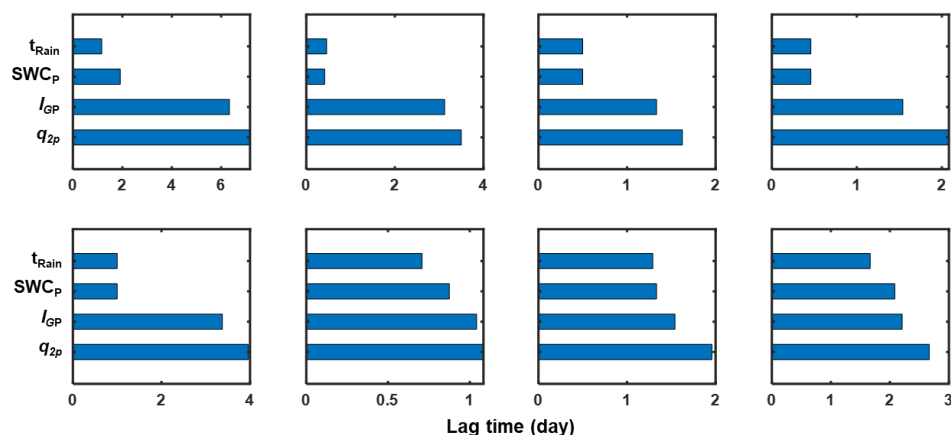
Figure 13. Lag times of maximum soil water content and groundwater level relative to rainfall onset. The beginning and end of each colored bar indicate the rise and peak times of according variable. SWC_{SP} is maximum soil water content. I_{GP} is the maximum I_G and q_{2p} is the delayed streamflow peak.

Rainfall duration across events ranged from 0.46 to 1.67 days. SWC, I_G, and delayed stormflow (q_{2p}) successively reached their peak values following the onset of a storm. SWC responded rapidly to rainfall, with its peak occurring 0.4 to 2.1 days after the storm began, typically coinciding with or slightly after the end of the rainfall. I_G continued to increase after the SWC peak, reaching its maximum before the peak in q_{2p}. The lag times from the SWC_p to the I_{Gp} and q_{2p} varied considerably across events. However, the lag time between I_{Gp} and q_{2p} was relatively consistent across events. As the prior research of Haught and Meerveld (2011) and Rinderer et al. (2016), who reported that identical or earlier response timing of groundwater compared to streamflow implies that a robust hillslope-stream connectivity is established and the streamflow response is driven by hillslope groundwater. Our results reinforce this understanding, as the timing of q_{2p} was predominantly governed by changes in groundwater. This conclusion is further corroborated by the strong linear correlation between the lag times of q_{2p} (t_{2p}) and I_{Gp} (t_{IGp}), as indicated by the regression equation t_{2p} = 1.11× t_{IGp} + 0.17, with a slope of 1.11, a determination coefficient R^2 = 0.995, and a t-test significance at the 0.01 level. (Fig. 14). Conversely, the correlation between t_{2p} and SWC_p (t_{SWCp}) was weak, with R^2 = 0.029 and a t-test significance level of 0.688, well above the 0.05 threshold,

398   indicating that t_{SWCp} has a negligible impact on t_{2p}. Additionally, as shown in Fig. A1, the I_G process

399   lines during the delayed stormflow period closely mirrored the shape of the streamflow hydrograph,

400   further emphasizing the dominant role of I_G in controlling q_{2p}.
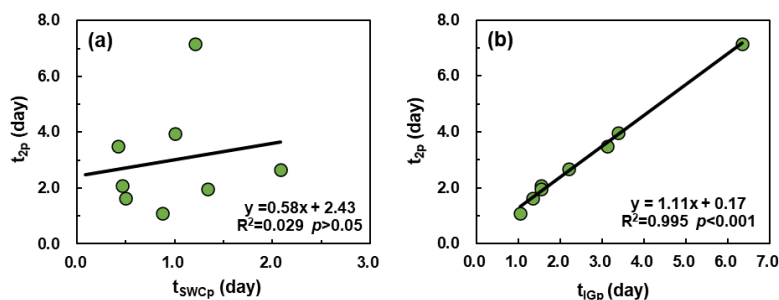
Figure 14. Lag times of maximum (a) SWC and (b) I_G in relation to the lag times of delayed
streamflow peaks (t_{2p}). t_{SWCp} and t_{IGp} are the occurrence times of the maximum soil water content
and maximum I_G, respectively.

405   The delayed stormflow process was quantitatively analyzed in relation to I_G variations during

406   this phase. As shown in Fig. 15, during the delayed stormflow period (i.e., non-rainfall period) of the

407   eight bimodal events, streamflow demonstrated a strong exponential relationship with increases in

408   GWL (IG_p), with a highly significant correlation ($p < 0.001$) and a correlation coefficient of $R^2 = 0.90$.

409   This exponential rise in streamflow corresponding to the increase in GWL can be attributed to a

410   potential enhancement in lateral hydraulic conductivity as the water table approaches the land surface,

411   consistent with findings by Detty and McGuire (2010) and Kendall et al. (1999). Furthermore, the

412   rapid increase in streamflow as the water table enters the surficial zone flattens the GWL vs.

413   streamflow curve, indicating the occurrence of transmissivity feedback. This feedback mechanism

414   led to a rise in GWL, which mobilized groundwater outflow, facilitating rapid transport via shallow

415   flow paths to the stream, as described by Lundin (1982).
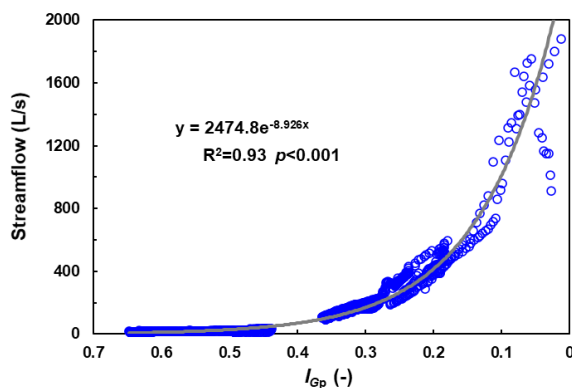
Figure 15. Correlation between I_G and streamflow during delayed stormflow periods.

4.3 Initiation of delayed stormflow triggered by soil water storage

Understanding the activation thresholds that govern water movement is crucial, as emphasized by McDonnell et al. (2021). Previous analyses in this study identified a strong correlation between delayed stormflow and the slow response of GWL. This slow response is triggered by a rapid decline in SWC, which only occurs when SWC exceeds a critical threshold of 0.20. To pinpoint the control threshold for delayed stormflow in XEW, we analyzed 63 out of 95 rainfall-runoff events that had complete SWC and GWL data. The relationship between SWCp and q_s for these events is illustrated in Fig. 16. A distinct threshold phenomenon was observed: q_s remained minimal when SWC was below 0.20, a condition prevalent in nearly all unimodal events. However, when SWC surpassed 0.20, there was a sudden increase in q_s due to the emergence of delayed stormflow in some events. Notably, when SWC exceeded 0.23, a significant surge in stormflow volume occurred, with a second stormflow peak appearing in all events. This suggests that an SWC range of 0.20 to 0.23 reflects the soil layer's water storage capacity, serving as a critical threshold for the onset of delayed stormflow.

431
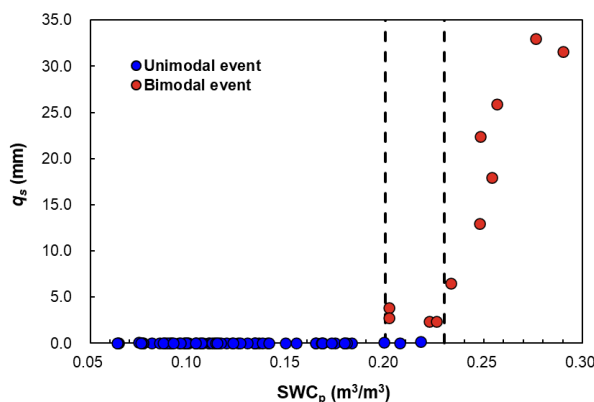
Figure 16. Relationship between maximum soil water content (SWC$_p$) and event stormflow amount (q_s).

These findings highlight the pivotal role of the surface soil layer's water deficit or water-holding capacity in determining the rainfall threshold for delayed stormflow initiation. During rainfall events, rainwater was largely retained within the soil layer until the amount exceeded its water-holding capacity. Furthermore, the analysis revealed that despite fluctuations in SWC, the q_s generated during unimodal events consistently remained below 1 mm, indicating that stormflow in these cases was mainly due to direct rainfall interception by the channel. Given the varying soil layer depths across the watershed, more detailed data on soil depth and distribution are essential for accurately estimating watershed-wide soil water storage capacity. However, observations of SWC across different locations show minimal variability within the watershed, suggesting that SWC serves as a reliable indicator of soil water storage in this study.

4.4 Conceptual model of runoff generation mechanism in XEW

In this section, we present a conceptual model that elucidates the mechanisms of runoff generation in the XEW watershed, with a focus on the role of soil water storage and GWL dynamics. Soil water storage is identified as the critical factor driving the transition from initial to delayed runoff generation. Once the soil water deficit is replenished, the slowly rising GWL becomes the primary control on the delayed stormflow process. Fig 17 illustrates the conceptual model of runoff generation, which incorporates transmissivity feedback mechanisms to explain the formation of distinct

24

451 hydrographs.

**1. Runoff generation under dry conditions (Fig. 17b):**

453 When the watershed is relatively dry and experiences light rainfall, the model shows that

454 rainwater primarily infiltrates and is stored within the soil layer. During such events, the streamflow

455 is composed of two main components: (1) a rapid streamflow peak resulting from direct rainfall on

456 the channel and (2) baseflow originating from the gradual release of deep groundwater. This baseflow

457 contribution is relatively constant, reflecting the slow discharge of groundwater from deeper aquifers.

2. Delayed stormflow during moderate storms (Fig. 17c):

459 In more substantial storm events, the soil water storage capacity is exceeded after the soil water

460 deficit is fully replenished. The initial response is similar to the dry condition scenario, with a rapid

461 streamflow peak generated by direct rainfall on the channel. However, as rainfall continues, the excess

462 water infiltrates deeply, elevating the GWL and expanding the effective connection area between the

463 stream channel and adjacent hillslopes. This vertical expansion of the saturated zone allows a

464 significant volume of shallow groundwater to be rapidly conveyed to the channel as the GWL reaches

465 a more conductive soil layer. The result is a delayed stormflow peak, which occurs after the rainfall

466 has ended.

3. Runoff generation during extreme storm events (Fig. 17d):

468 In extreme storm events characterized by substantial rainfall input, GWLs rise sharply across

469 the entire watershed, reaching levels associated with higher hydraulic conductivity. This synchronous

470 rise in GWL triggers the rapid release of a large volume of shallow groundwater, leading to a

471 significant flood peak within a short time frame. During these events, the GWL in the riparian zone

472 may rise into the soil layer or even reach the ground surface, facilitating water movement into the

473 channel via soil subsurface flow. Observations from extreme storm events support this mechanism,

474 as the deeper soil layer in the riparian zones often shows a sudden and sustained increase in SWC

475 after rainfall has ceased, suggesting that groundwater from adjacent hillslopes may be replenishing

476 soil water in these areas.
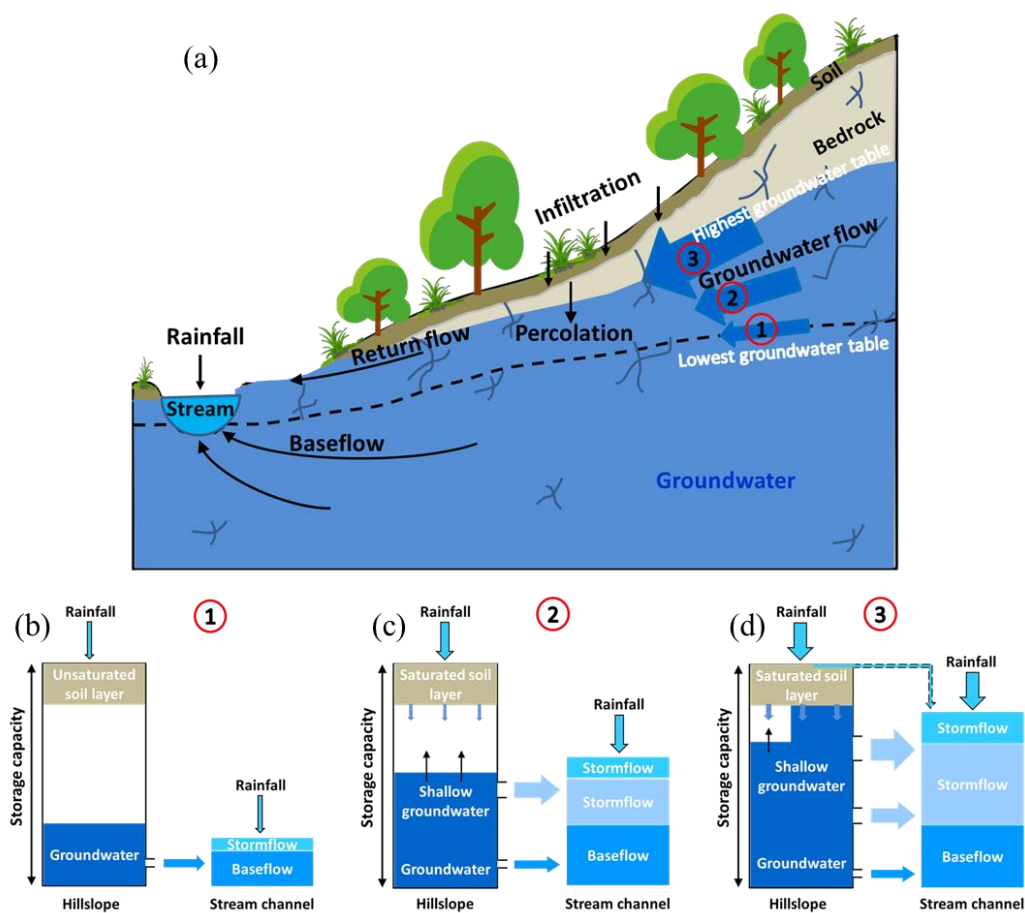
Figure 17. Conceptual model illustrating the stormflow generation associated with the transmissivity feedback.

The transition from the runoff generation model depicted in Fig. 17b to Fig. 17c and ultimately Fig. 17d corresponds to a progressive wetting-up of the watershed. The abrupt changes in stormflow volume and timing are initially triggered by soil water storage and later governed by the hydraulic conductivity of the bedrock and micro-topography. This conceptual model provides a quantitative framework for understanding how varying hydrological conditions influence the runoff generation processes in the XEW watershed.

5. Conclusions

486

487   Building upon previous work that identified and characterized bimodal streamflow patterns in
488   the XEW watershed, this study provides a detailed, quantitative analysis of SWC and GWL at the
489   event scale to elucidate the mechanisms behind delayed stormflow generation. The findings reveal
490   that when soil water storage surpasses its holding capacity, a secondary increase in streamflow is
491   triggered. This secondary, or delayed, stormflow is primarily governed by GWL dynamics,
492   influencing both the magnitude of delayed stormflow and the lag time to its peak.

493   During rainfall events, SWC exhibits a rapid response, continuing to increase until it reaches or
494   exceeds the soil's water storage capacity. If the stored water remains within this capacity, SWC
495   stabilizes or decreases slowly after rainfall ceases, eventually leveling off near the field capacity. The
496   rate of SWC decrease is directly proportional to the extent to which it exceeds field capacity. When
497   SWC decreases, excess rainwater infiltrates deeper into the soil, raising the GWL. Once the GWL
498   begins to rise, it becomes the dominant factor driving the delayed stormflow process.

499   As GWL rises, hydraulic conductivity increases, allowing more groundwater to flow from
500   hillslopes into the channel, thereby forming delayed stormflow. This process also causes the effective
501   connection area between the stream channel and adjacent hillslopes to expand vertically. At specific
502   high GWL thresholds, the synchronization of GWL responses across multiple hillslopes leads to a
503   substantial increase in stormflow volume. This synchronized response shortens the lag time and
504   increases the volume of delayed stormflow, often causing the delayed stormflow peak to merge with
505   the direct stormflow peak.

506   These findings provide a deeper understanding of the nonlinear behavior of stormflow and the
507   mechanisms behind the formation of bimodal hydrographs. This enhanced understanding has
508   significant implications for advancing hydrological theory and offers valuable insights for improving
509   and optimizing flood modeling and prediction.

Data availability

All the data used in this study will be available at the Zenodo website at the time of publication.

Author contribution

ZC contributed the conceptualization, formal analysis, investigation and writing; FT contributed the conceptualization, formal analysis and revision.

Competing interests

Fuqiang Tian is a members of the editorial board of Hydrology and Earth System Sciences.

Acknowledgements

5. References

Ali, G., Oswald, C. J., Spence, C., Cammeraat, E. L., McGuire, K. J., Meixner, T., and Reaney, S. M.: Towards a unified threshold-based hydrological theory: necessary components and recurring challenges, Hydrol. Process., 27, 313–318, https://doi.org/10.1002/hyp.9560, 2013.

Anderson, M. G., and Burt, T. R.: The role of topography in controlling throughflow generation, Earth Surf. Process., 3, 331–334, https://doi.org/10.1002/esp.3290030402, 1978.

Beiter, D., Weiler, M., and Blume, T.: Characterising hillslope–stream connectivity with a joint event analysis of stream and groundwater levels, Hydrol. Earth Syst. Sci., 24, 5713-5744, https://doi.org/10.5194/hess-24-5713-2020, 2020.

Bishop, K., Seibert, J., Nyberg, L., and Rodhe, A.: Water storage in a till catchment. II: Implications of transmissivity feedback for flow paths and turnover times, Hydrol. Process., 25, 3950-3959, https://doi.org/10.1002/hyp.8355, 2011.

Cain, M. R., Woo, D. K., Kumar, P., Keefer, L., and Ward, A. S.: Antecedent conditions control thresholds of tile-runoff generation and nitrogen export in intensively managed landscapes, Water Resour. Res., 58, e2021WR030507, https://doi.org/10.1029/2021WR030507, 2022.

Cui, Z., Tian, F., Zhao, Z., Xu, Z., Duan, Y., Wen, J., and Khan, M. Y. A.: Bimodal Hydrographs in Semi-humid

Forested Watershed: Characteristics and Occurrence Conditions, Hydrol. Earth Syst. Sci. Discuss., https://doi.org/10.5194/hess-2024-36, 2024.

Dang, L., Xie, Y. Q., Wang, C., Chang, Y., Zeng, X. K., and Wu, J. C.: Precipitation-induced Pressure Wave Propagation in Unsaturated Zone and Its Effect on Rapid Groundwater Discharge, Geol. J. China Univ., 29, 580-589, https://doi.org/10.16108/j.issn1006-7493.2021104, 2023.

Detty, J. M., and McGuire, K. J.: Threshold changes in storm runoff generation at a till-mantled headwater catchment, Water Resour. Res., 46, W07525, https://doi.org/10.1029/2009WR008102, 2010.

Farrick, K. K., and Branfireun, B. A.: Soil water storage, rainfall and runoff relationships in a tropical dry forest catchment, Water Resour. Res., 50, 9236-9250, https://doi.org/10.1002/2014WR016045, 2014.

Fu, C., Chen, J., Jiang, H., and Dong, L.: Threshold behavior in a fissured granitic catchment in southern China: 1. Analysis of field monitoring results, Water Resour. Res., 49, 2519-2535, https://doi.org/10.1002/wrcr.20193, 2013.

Graeff, T., Zehe, E., Reusser, D., Lück, E., Schröder, B., Wenk, G., John, H., and Bronstert, A.: Process identification through rejection of model structures in a mid-mountainous rural catchment: observations of rainfall-runoff response, geophysical conditions and model inter-comparison, Hydrol. Process., 23, 702–718, https://doi.org/10.1002/hyp.7171, 2009.

Graham, C. B., and McDonnell, J. J.: Hillslope threshold response to rainfall: (2) development and use of a macroscale model, J. Hydrol., 393, 77–93, https://doi.org/10.1016/j.jhydrol.2010.03.008, 2010.

Graham, C. B., Woods, R. A., and McDonnell, J. J.: Hillslope threshold response to rainfall: (1) A field based forensic approach, J. Hydrol., 393, 65–76, https://doi.org/10.1016/j.jhydrol.2009.12.015, 2010.

Haga, H., Matsumoto, Y., Matsutani, J., Fujita, M., Nishida, K., and Sakamoto, Y.: Flow paths, rainfall properties, and antecedent soil moisture controlling lags to peak discharge in a granitic unchanneled catchment, Water Resour. Res., 41, W2179–W2187, https://doi.org/10.1029/2005wr004236, 2005.

Haught, D. R. W. and Meerveld, H. J.: Spatial variation in transient water table responses: differences between an upper and lower hillslope zone, Hydrol. Process., 25, 3866-3877, https://doi.org/10.1002/hyp.8354, 2011.

Jin, Z., Guo, L., Yu, Y., Luo, D., Fan, B., and Chu, G.: Storm runoff generation in headwater catchments on the Chinese Loess Plateau after long-term vegetation rehabilitation, Sci. Total Environ., 748, 141375, https://doi.org/10.1016/j.scitotenv.2020.141375, 2020.

Kendall, K. A., Shanley, J. B., and McDonnell, J. J.: A hydrometric and geochemical approach to test the transmissivity feedback hypothesis during snowmelt, J. Hydrol., 219, 188–205, https://doi.org/10.1016/S0022-1694(99)00059-1, 1999.

Kosugi, K., Fujimoto, M., Katsura, S., Kato, H., Sando, Y., and Mizuyama, T.: Localized bedrock aquifer distribution explains discharge from a headwater catchment, Water Resour. Res., 47, W07111, https://doi.org/10.1029/2010WR009884, 2011.

Martínez-Carreras, N., Hissler, C., Gourdol, L., Klaus, J., Juilleret, J., Iffly, J. F., and Pfister, L.: Storage controls on the generation of double peak hydrographs in a forested headwater catchment, J. Hydrol., 543, 255–269,

572   https://doi.org/10.1016/j.jhydrol.2016.10.004, 2016.

573   McDonnell, J. J., Spence, C., Karran, D. J., Van Meerveld, H. J., and Harman, C. J.: Fill-and-spill: A process

574   description of runoff generation at the scale of the beholder, Water Resour. Res., 57, e2020WR027514,

575   https://doi.org/10.1029/2020WR027514, 2021.

576   McGuire, K. J., and McDonnell, J. J.: Hydrological connectivity of hillslopes and streams: characteristic time scales

577   and nonlinearities, Water Resour. Res., 46, W10530, https://doi.org/10.1029/2010WR009341, 2010.

578   Padilla, C., Onda, Y., and Iida, T.: Interaction between runoff–bedrock groundwater in a steep headwater catchment

579   underlain by sedimentary bedrock fractured by gravitational deformation, Hydrol. Process., 29, 4398–4412,

580   https://doi.org/10.1002/hyp.10498, 2015.

581   Penna, D., Tromp-van Meerveld, H. J., Gobbi, A., Borga, M., and Dalla Fontana, G.: The influence of soil moisture

582   on threshold runoff generation processes in an alpine headwater catchment, Hydrol. Earth Syst. Sci., 15, 689-

583   702, https://doi.org/10.5194/hess-15-689-2011, 2011.

584   Phillips, J. D.: Sources of nonlinearity and complexity in geomorphic systems, Prog. Phys. Geogr., 27, 1-23,

585   https://doi.org/10.1191/0309133303pp340ra, 2003.

586   Rinderer, M., van Meerveld, I., Stähli, M., and Seibert, J.: Is groundwater response timing in a pre-alpine catchment

587   controlled   more   by   topography   or   by   rainfall?   Hydrol.   Process.,   30,   1036-1051,

588   https://doi.org/10.1002/hyp.10634, 2016.

589   Ross, C. A., Ali, G. A., Spence, C., and Courchesne, F.: Evaluating the Ubiquity of Thresholds in Rainfall‐Runoff

590   Response   Across   Contrasting   Environments,   Water   Resour.   Res.,   57,   e2020WR027498,

591   https://doi.org/10.1029/2020WR027498, 2021.

592   Sakakibara, K., and Suzuki, K.: Controlling Factors and Characteristics of Peak Runoff in an Alpine Headwater

593   Under the Asian Monsoon Climate, Mt. Res. Dev., 42, R1–R8, https://doi.org/10.1659/MRD-JOURNAL-D-

594   21-00030.1, 2022.

595   Scaife, C. I., and Band, L. E.: Nonstationarity in threshold response of stormflow in southern Appalachian headwater

596   catchments, Water Resour. Res., 53, 6579-6596, https://doi.org/10.1002/2017WR020376, 2017.

597   Scaife, C. I., Singh, N. K., Emanuel, R. E., Miniat, C. F., and Band, L. E.: Non-linear quickflow response as

598   indicators   of   runoff   generation   mechanisms,   Hydrol.   Process.,   34,   2949–2964,

599   https://doi.org/10.1002/hyp.13780, 2020.

600   Sivapalan, M.: Process complexity at hillslope scale, process simplicity at watershed scale: Is there a connection,

601   Hydrol. Process., 17, 1037-1041, https://doi.org/10.1002/wrcr.20193, 2003.

602   Sloto, R. A., and Crouse, M. Y.: HYSEP: A computer program for streamflow hydrograph separation and analysis,

603   US Geol. Surv., https://doi.org/10.3133/wri964040, 1996.

604   Tian, F., Li, H., and Sivapalan, M.: Model diagnostic analysis of seasonal switching of runoff generation

605   mechanisms   in   the   blue   river   basin,   Oklahoma,   J.   Hydrol.,   418-419,   136–149,

606   https://doi.org/10.1016/j.jhydrol.2010.03.011, 2012.

607   Tie, Q., Hu, H., Tian, F., and Holbrook, N. M.: Comparing different methods for determining forest

608   evapotranspiration and its components at multiple temporal scales, Sci. Total Environ., 633, 12–29,

609   https://doi.org/10.1016/j.scitotenv.2018.03.082, 2018.

610 Tromp-van Meerveld, H. J., and McDonnell, J. J.: Threshold relations in subsurface stormflow: 1. A 147-storm

611   analysis of the Panola hillslope, Water Resour. Res., 42, W02410, https://doi.org/10.1029/2004WR003778,

612   2006a.

613 Tromp-van Meerveld, H. J., and McDonnell, J. J.: Threshold relations in subsurface stormflow: 2. The fill and spill

614   hypothesis, Water Resour. Res., 42, W02411, https://doi.org/10.1029/2004WR003800, 2006b.

615 Uchida, T., Tromp-van Meerveld, I., and McDonnell, J. J.: The role of lateral pipe flow in hillslope runoff response:

616   an intercomparison of non-linear hillslope response, J. Hydrol., 311, 117-133,

617   https://doi.org/10.1016/j.jhydrol.2005.01.012, 2005.

618 Zhang, G., Cui, P., Gualtieri, C., Zhang, J., Bazai, N. A., Zhang, Z., Wang, J., Tang, J. B., Chen, R., and Lei, M.:

619   Stormflow generation in a humid forest watershed controlled by antecedent wetness and rainfall amounts, J.

620   Hydrol., 603, 127107, https://doi.org/10.1016/j.jhydrol.2021.127107, 2021.

621

622   **Appendix A:**
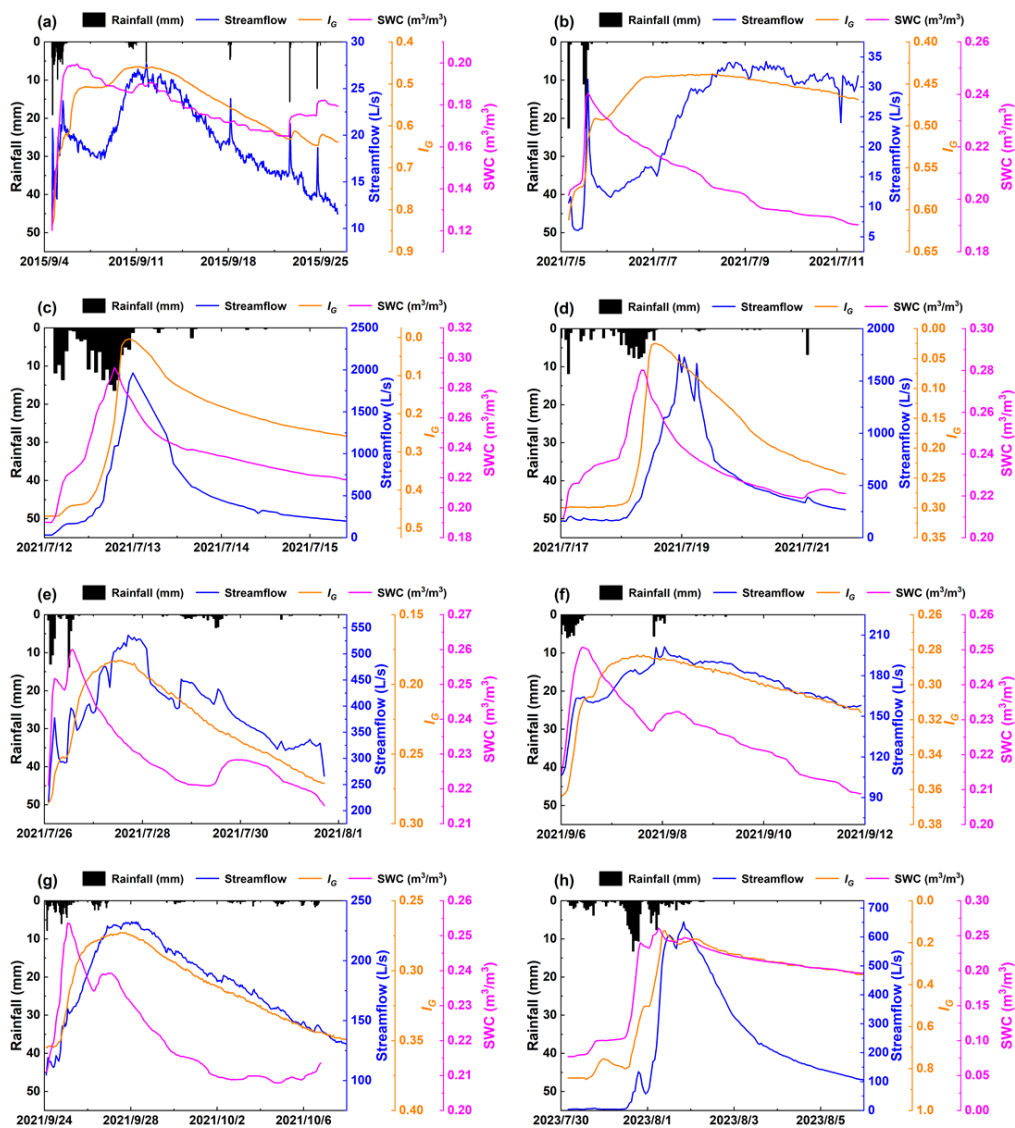
623

624   **Figure A1.** Examples of responses of streamflow, IG and soil water content to rainfall.